JOURNAL OF SOLID STATE CHEMISTRY 85, 202–219 (1990)

A Structural Study of the Incorporation of Silica into Sodium Ferrites, $Na_{1-x}[Fe_{1-x}Si_xO_2]$, $x = 0$ to 0.20

IAN E. GREY,* BERNARD F. HOSKINS,† AND IAN C. MADSEN

CSIRO, Division of Mineral Products, P.O. Box 124, Port Melbourne, Victoria 3207, Australia

Received June 30, 1989; in revised form October 30, 1989

Rietveld refinements of X-ray powder intensity data have been performed for solid solution phases along the $NaFeO_2$–SiO_2 join. Five compositions $Na_{1-x}[Fe_{1-x}Si_xO_2]$ with $x = 0$ to 0.10 (β_{ss}, isostructural with β-$NaFeO_2$) and four with $x = 0.125$ to 0.20 (γ'_{ss}, isostructural with $KGaO_2$) were refined. The results were used to analyze the effect of incorporation of silica into $NaFeO_2$ on the rotation of the cristobalite-type tetrahedral framework and the associated changes in the environment of the sodium atoms. In the γ'_{ss}-solid solution series, there is partial ordering of iron and silicon in the tetrahedral framework, with an associated modulation of the sodium atom distribution.

1. Introduction

We have recently reported the results of a phase equilibria study of the pseudobinary join $NaFeO_2$–SiO_2 (*1*). The study was undertaken as part of a general project on the DARS (Direct Alkali Recovery System) process for caustic regeneration from spent paper pulp liquors (*2*). In this process, spent pulp liquors are roasted with hematite to form sodium ferrite, $NaFeO_2$, which is then hydrolyzed to produce NaOH solution and iron oxide that is recycled to the roaster. When silica is present, from the hematite or the spent liquor, it is incorporated into the sodium ferrite and it determines the amount of sodium that can be extracted in the hydrolysis stage. The amount of hydrolysis-resistant sodium has a linear relationship to the silica content, and so silica impurities limit the efficiency of the process.

We were interested to determine if the effect of silica on the sodium hydrolysis could be explained structurally, in terms of modifications to the sodium site coordination and potential sodium diffusion paths resulting from the substitution of silica into $NaFeO_2$. The detailed structural information needed as data for this approach was obtained by Rietveld refinement of X-ray powder intensity data for compounds along the $NaFeO_2$–SiO_2 join. Our previous phase equilibria studies (*1*) had shown that for samples cooled to room temperature a solid solution with the β-$NaFeO_2$ structure is stable for compositions with 0 to 11 mol% SiO_2. At higher SiO_2 contents, a new orthorhombic solid solution phase, γ'_{ss}, is

* To whom correspondence should be addressed.

† Permanent address: Department of Inorganic Chemistry, University of Melbourne, Parkville, Victoria 3052, Australia.

0022-4596/90 $3.00

stable. The γ'_{ss} phase has an X-ray diffraction pattern and cell dimensions similar to those for $KGaO_2$ (*3*).

The γ-form of $NaFeO_2$, and a new cubic polymorph, δ-$NaFeO_2$ (*1*), also forms solid solutions with SiO_2, but these phases are only stable at elevated temperatures, and transform rapidly to the β_{ss} or γ'_{ss} forms on cooling (*1*). We report here the results of Rietveld refinements for members of the β_{ss} series with 0, 2.5, 5, 7.5, and 10 mol% SiO_2 and for members of the γ'_{ss} series with 12.5, 15, 17.5, and 20 mol% SiO_2.

2. Experimental

2.1. Preparation of Solid Solutions

All solid solutions described below were prepared using Fisher certified Fe_2O_3, BDH analytical-grade sodium oxalate, and BDH laboratory reagent-precipitated silica. The Fe_2O_3 and $Na_2C_2O_4$ were dried at 700 and 105°C, respectively, and stored in a desiccator. The water content of the precipitated silica was determined by weight loss on heating to constant weight at 900°C. All of the solid solution preparations were stored in a desiccator over silica gel to prevent hydrolysis.

For the preparation of the β_{ss} phases $Na_{1-x}[Fe_{1-x}Si_xO_2]$, $x = 0$, 0.025, 0.050, 0.075, and 0.100, stoichiometric amounts of Fe_2O_3, $Na_2C_2O_4$, and $SiO_2 \cdot nH_2O$ were intimately ground, placed in a Pt crucible, heated at 750°C for 1 hr, cooled, reground, and reheated for approximately 16 to 20 hr at 750°C. The samples were again cooled and reground, and then heated to 1000°C for 2 hr; the last mentioned step was repeated.

The preparation of the γ'_{ss} phases $Na_{1-x}[Fe_{1-x}Si_xO_2]$, $x = 0.125$, 0.150, 0.175, and 0.200, involved similar preliminary heat treatments as for the β_{ss} phases. However, after the second heating at 1000°C the samples were annealed overnight (18.5 to 20 hr) at 850°C for $x = 0.125$, 800°C for $x = 0.150$ and 0.175, and 750°C for $x = 0.200$.

2.2. X-Ray Diffraction Powder Patterns

The X-ray powder diffraction (XRD) patterns were recorded for each sample using a Philips PW1050 goniometer/PW1710 controller equipped with a graphite postdiffraction monochromater. The specimens with $x = 0.0$ to 0.10 possess diffraction patterns characteristic of the β_{ss} solid solutions (*1*) and showed no evidence of the presence of any other phase or any of the starting materials. The γ'_{ss} solid solutions ($x = 0.125$, 0.150, 0.175, and 0.200) yield XRD patterns characteristic of their phase type (1) and again there was no evidence of any of the starting materials. It was subsequently shown, during the Rietveld refinement, that the phase with $x = 0.125$, although predominantly a γ'_{ss} solid solution, contained a minor amount (approx 5 mol%) of the β_{ss} form.

2.3. X-Ray Data Collection

Step-scan X-ray powder intensity data were obtained at 24°C with a Philips PW1050 goniometer/PW1710 controller. Intensity measurements in the 2θ ranges of 15.0 to 105.0° and 15.0 to 90.0° for the β_{ss} and γ'_{ss} solid solutions, respectively, were made at intervals of 0.04° using Cu$K\alpha$ radiation and a step-counting time of 5 sec. The X-ray tube was operated at 45 kV and 30 mA, with 1° divergence and receiving slits, a 1° scatter slit, and divergent and diffracted beam soller slits.

2.4. Structure Refinement

Least-squares structure refinements were carried out using the Rietveld DBW3.2 analysis program (*4*), which has been modified to include the application of a 2θ-variable pseudo-Voigt peak shape function (*5*). Profile refinement parameters included a scale factor, three pseudo-Voigt shape parameters, a 2θ zero parameter, a

peak full-width at half-maximum (FWHM) function of the form $FWHM^2 = U \tan^2 \theta + V \tan \theta + W$, where U, V, and W are refinable parameters (*6*), calculated for 7.0 half-widths on either side of the peak maximum, a peak asymmetry parameter for angles less than 24° (*7*), and the unit cell dimensions. All the refinements included a refinement of the background using a five-parameter polynomial in $2\theta^n$ where n has the values from 0 to 4 inclusive. An experimentally determined value of 0.91 was used for the monochromator polarization correction (*8*). Neutral atom scattering factors, including anomalous dispersion corrections, were taken from Ref. (*9*).

2.5. Crystal Structure of β_{ss} Solid Solutions

The reported (*10*) unit cell data and atomic coordinates for β-$NaFeO_2$, given in Table I, were used to initiate the Rietveld refinement of pure β-$NaFeO_2$. The refined parameters included the profile parameters described above and isotropic thermal parameters. Convergence was considered achieved when the parameter shift was less than 0.25 ESD. The refined cell parameters, atomic coordinates, and thermal parameters together with the values for R_{wp} and R_B are given in Table II. A list of the step intensity data may be obtained from the authors for this and all subsequent refinements. The parameters obtained for the pure β-$NaFeO_2$ were used as the starting values for the Rietveld refinements of the β_{ss} solid solutions; the resulting atomic coordinates and cell parameters are also included in Table II. For each refinement the site occupation factors of the Na and the mixed Si/Fe sites were fixed at values corresponding to the molar quantity of each and the y-coordinates of all atoms were referred to that of the Fe or mixed Fe/Si site which was fixed at 0.0 throughout the refinement. The observed, calculated, and difference profile for the solid solution where $x = 0.025$ is given in Fig. 1a.

TABLE I

STRUCTURAL DATA FOR β-$NaFeO_2$ FROM REF. (*10*)[a]

Atom	x	y	z
Fe	0.062	0.0	0.130
Na	0.416	−0.489	0.151
O(1)	0.043	−0.339	0.084
O(2)	0.380	0.073	0.153

[a] Coordinates and unit cell transformed to the space group setting $Pn2_1a$. Crystal data: orthorhombic, a = 5.672, b = 5.377, and c = 7.136 Å, with four formula units per unit cell.

2.6. Crystal Structure of the γ'_{ss} Solid Solutions

Crystals of members of the γ'_{ss} series obtained by the slow cooling from the melt were studied using precession and Weissenberg single crystal methods. The diffraction patterns could be indexed in terms of a tetragonal superlattice of cubic high-cristobalite with $a_t = \sqrt{2}a_c$ and $c_t = 2a_c$. However, the diffraction patterns could also be interpreted in terms of multiple orientations of an orthorhombic cell with $a_o = \frac{1}{2} a_t$ as for $KGaO_2$ (*1*, *3*), which is a superstructure of high-cristobalite. We were unable to produce single crystals of the γ'_{ss} phase of only one orientation and so it was decided to embark on Rietveld refinements of powder data for the γ'_{ss} solid solutions using the $KGaO_2$ structure as the starting model. The solid solution with $x = 0.175$ was chosen for the first study. The initial unit cell parameters used were those obtained during the phase study of the $NaFeO_2$–SiO_2 system (*1*). Attempts to initiate a satisfactory Rietveld refinement using the literature values given for the atomic coordinates of the $KGaO_2$ structure (*3*) soon indicated that some of these parameters must be in error. An examination of the interatomic distances and angles using the reported coordinates revealed a typographical error for

TABLE II

RIETVELD REFINEMENT RESULTS FOR β_{ss}-SOLID SOLUTIONS OF COMPOSITION $Na_{1-x}[Fe_{1-x}Si_xO_2]$

		x in $Na_{1-x}[Fe_{1-x}Si_xO_2]$				
		0.00	0.025	0.050	0.075	0.100
				Unit cell data		
a(Å)		5.6731(2)	5.6454(2)	5.6328(2)	5.6031(2)	5.5727(4)
b(Å)		5.3853(2)	5.3765(2)	5.3744(2)	5.3665(2)	5.3615(4)
c(Å)		7.1440(2)	7.1544(2)	7.1604(3)	7.1715(3)	7.1845(6)
U(Å^3)		218.26(2)	217.15(2)	216.77(2)	215.64(2)	214.66(5)
				Atomic coordinates and B(Å^2) values		
Fe/Si	x	0.0672(4)	0.0672(3)	0.0661(4)	0.0640(3)	0.0615(5)
	y	0.0(—)	0.0(—)	0.0(—)	0.0(—)	0.0(—)
	z	0.1280(6)	0.1264(5)	0.1266(6)	0.1266(6)	0.1284(8)
	B	0.31(5)	0.21(5)	0.29(6)	0.28(6)	0.31(10)
Na	x	0.4248(8)	0.4281(8)	0.4293(9)	0.4305(7)	0.4340(12)
	y	−0.484(2)	−0.480(2)	−0.480(2)	−0.478(2)	−0.477(3)
	z	0.123(2)	0.123(1)	0.122(2)	0.124(1)	0.124(2)
	B	1.01(14)	0.82(14)	0.95(17)	0.74(14)	0.53(24)
O(1)	x	0.043(2)	0.046(2)	0.047(2)	0.040(2)	0.040(2)
	y	−0.341(1)	−0.341(1)	−0.342(1)	−0.341(1)	−0.345(2)
	z	0.092(2)	0.088(2)	0.089(2)	0.084(2)	0.089(2)
	B	0.51(30)	0.43(27)	0.75(33)	0.55(27)	0.09(42)
O(2)	x	0.390(2)	0.386(1)	0.382(1)	0.381(1)	0.372(2)
	y	0.079(2)	0.079(1)	0.078(2)	0.078(1)	0.075(2)
	z	0.157(2)	0.160(2)	0.162(2)	0.164(1)	0.173(2)
	B	1.49(37)	0.50(30)	0.61(35)	0.58(28)	0.39(42)
				Agreement indices		
R_{wp} (%)		12.70	11.77	14.12	11.25	16.29
R_B (%)		3.56	2.75	3.24	2.74	5.12
R_{exp} (%)		3.88	3.79	3.90	3.80	3.81

the x-coordinate of Ga(1). In addition it was clear that O(4) had been incorrectly located because of the unconvincing bond angles about Ga(1) involving this oxygen atom, which fell in the range 86 to 129°, as well as the unacceptably close O(4). . .O(2) contact of 2.45 Å.

A least-squares refinement (*11*) using the structure amplitude values (derived by photographic methods) and the atomic coordinates reported by Vielhaber and Hoppe (*3*), with the value of the x-coordinate for Ga(1) corrected to 0.261, did not improve these anomalous features. In addition there was a peak in the difference map of approximately 2.0 e Å^{-3} at bonding distance to Ga(1) suggesting an alternative site for O(4). This was confirmed from an ab initio redetermination of the structure, using direct and Fourier methods (*11*), with the new coordinates for O(4) resulting in all of the O–Ga–O bond angles falling in the range 106 to 114° and all the O. . .O contacts >2.87 Å. There was a significant improvement in both the R and R_w values as well; the refinement of Vielhaber and Hoppe's model gave values for R and R_w of 0.115 and 0.109, respectively, whereas that with O(4) shifted to the new site gave values for the corresponding parameters of

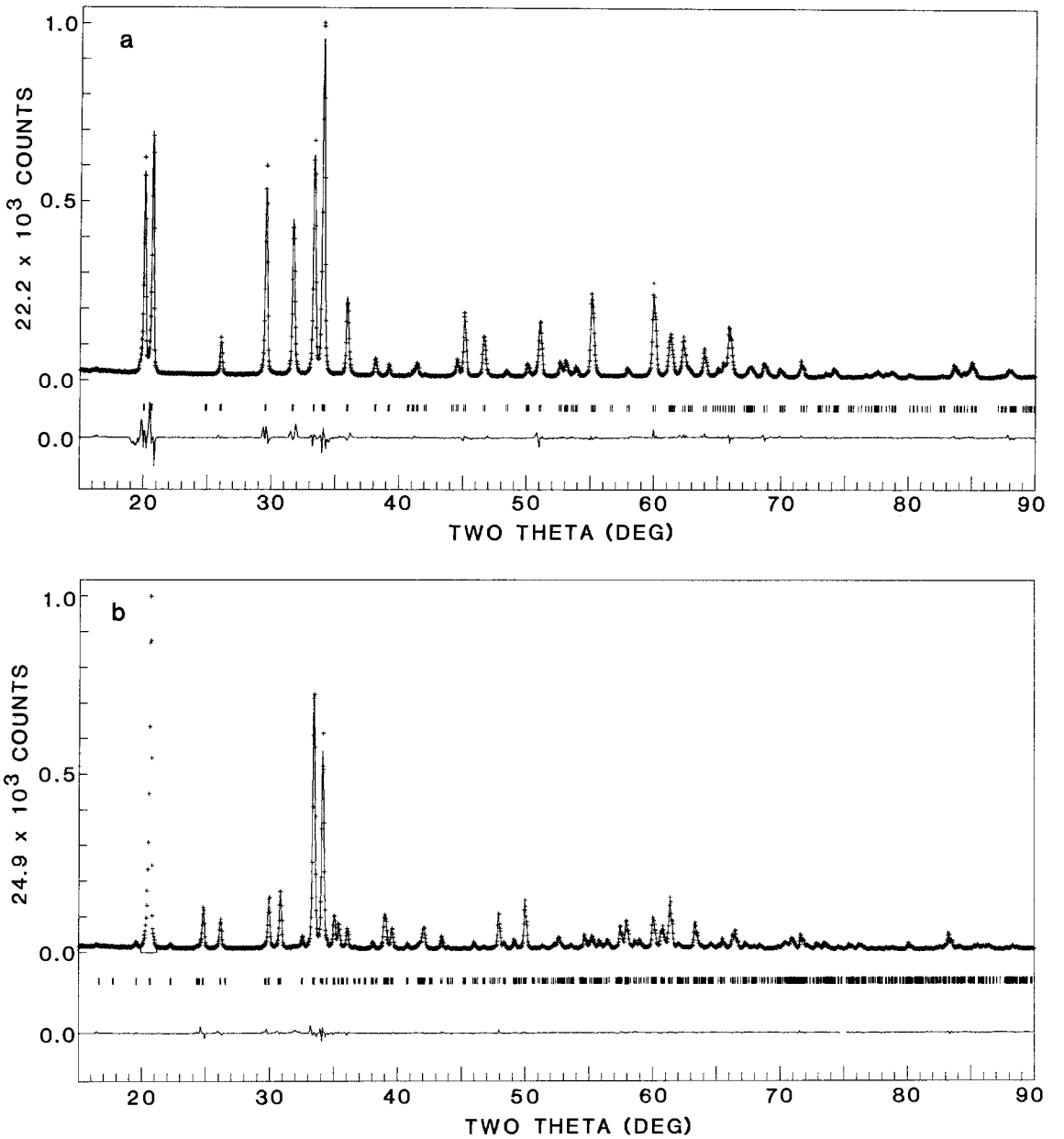

FIG. 1. Observed, calculated, and difference X-ray powder diffraction profile for (a) the β_{ss}-solid solution where $x = 0.025$ and (b) the γ'_{ss}-solid solution where $x = 0.150$. The observed data are indicated by points and the calculated profile by the continuous line. The short vertical lines below the profile represent the positions of all the possible Bragg reflections.

0.105 and 0.098. The atomic coordinates resulting from our refinement are given in Table III. It is worth noting that the values we have found for the atomic coordinates for the $KGaO_2$ structure are comparable to those reported for the Rietveld refinement

TABLE III

REVISED ATOMIC COORDINATES FOR $KGaO_2$[a]

Atom	x	y	z
Ga(1)	0.258(1)	0.0088(3)	0.1890(2)
Ga(2)	0.280(1)	0.2633(3)	0.0644(2)
K(1)	0.758(3)	0.0140(7)	0.0613(5)
K(2)	0.799(3)	0.2645(7)	0.1852(5)
O(1)	0.569(8)	0.302(2)	0.011(2)
O(2)	0.158(6)	0.406(2)	0.103(2)
O(3)	0.311(7)	0.164(2)	0.155(2)
O(4)	0.059(9)	0.479(3)	0.276(2)

[a] Crystal data (*3*): orthorhombic, space group *Pbca*, $a = 5.515$, $b = 11.076$, $c = 15.818$ Å, 16 formula units per unit cell.

parameters derived for $KFeO_2$ from a neutron diffraction study (*12*).

The revised atomic coordinates for the $KGaO_2$ structure proved to be a satisfactory starting point in the subsequent Rietveld refinement of the γ'_{ss} solid solutions with $x = 0.175$. At convergence the profile, unit cell, and atomic parameters yielded a calculated profile in good agreement with the observed data. An analogous refinement was carried out for each of the remaining solid solutions of the γ'_{ss} series using the parameters obtained for the $x = 0.175$ solid solution as the starting point. Using normal conditions of refinement the atomic parameters either diverged or refined to a model for which the calculated profile did not include a number of the weaker superlattice reflections, even though a satisfactory fit in terms of R_{wp} and R_B appeared to have been obtained. In order to achieve convergence and a model which gave a satisfactory fit between the observed and calculated profiles throughout the complete scan range it was found necessary to apply a severe dampening factor (0.1) to the calculated parameter shifts to allow the parameters to approach the converged values slowly over many (12 to 15) cycles of refinement. A common isotropic temperature factor was used for each atom type. For the final cycles of refinement all parameters were held constant except for the site occupation factors for the independent Fe/Si and Na/□ sites, where □ = Na vacancy.

The solid solution with $x = 0.125$ proved to contain a small amount of the β_{ss} form so that this sample was treated as a two component system for the Rietveld refinement; only the parameters for the γ'_{ss} have been reported in Table IV. It was found that for all of the γ'_{ss} solid solutions, with the exception of the sample containing 12.5 mol% of SiO_2, the peak in the observed profile at approximately 20.5° possessed asymmetry such that it could not be adequately modeled by the calculated profile. For this reason the region 19.9 to 21.0° was excluded from the Rietveld analysis for the solid solutions where $x = 0.150$, 0.175, and 0.200. The observed, calculated, and difference profiles for solid solution where $x = 0.150$ is shown in Fig. 1b.

The refined unit cell parameters, atomic coordinates and thermal parameters together with R_{wp}, R_B, and R_{exp} are given in Table IV.

3. Results and Discussion

3.1. β_{ss}-Solid Solutions

3.1.1. Tetrahedra rotations in the β series. Polyhedral representations of the structure of the β phase viewed along [010] are shown in Fig. 2. In Fig. 2a both the sodium- and iron-centered tetrahedra are drawn to show the structure as a distorted wurtzite superstructure; the view direction corresponds to $c_{wurtzite}$. In wurtzite the anions are in hexagonal close packing and all tetrahedra are the same size. The local substitution of Si for Fe and associated loss of Na from an adjacent tetrahedron in $Na_{1-x}[Fe_{1-x}Si_x]O_2$ is also shown in Fig. 2a.

In Fig. 2b only the iron-centered tetrahedra are shown, emphasizing the structural

TABLE IV

RIETVELD REFINEMENT RESULTS FOR γ'_{ss}-SOLID SOLUTIONS OF COMPOSITION $Na_{1-x}[Fe_{1-x}Si_xO_2]$

		x in $Na_{1-x}[Fe_{1-x}Si_xO_2]$			
		0.125	0.150	0.175	0.200
		Unit cell data			
a(Å)		5.3923(2)	5.3875(2)	5.3804(2)	5.3749(2)
b(Å)		10.7658(4)	10.7549(3)	10.7438(4)	10.7280(4)
c(Å)		14.6468(4)	14.6273(3)	14.6014(4)	14.5826(4)
U(Å^3)		850.28(9)	847.54(7)	844.05(9)	840.86(9)
		Atomic coordinates			
Fe/Si(1)	x	0.1909(9)	0.1939(6)	0.1953(7)	0.1941(7)
	y	0.0256(4)	0.0266(3)	0.0273(4)	0.0280(3)
	z	0.1886(4)	0.1879(3)	0.1877(4)	0.1886(3)
	SOF(Si)	0.11(2)	0.19(1)	0.19(2)	0.24(1)
Fe/Si(2)	x	0.3079(8)	0.3087(6)	0.3055(7)	0.3079(7)
	y	0.2758(4)	0.2767(3)	0.2766(4)	0.2764(4)
	z	0.0601(4)	0.0592(3)	0.0598(3)	0.0595(3)
	SOF(Si)	0.08(2)	0.15(1)	0.15(1)	0.19(1)
Na(1)	x	0.724(2)	0.713(2)	0.710(2)	0.714(2)
	y	−0.021(1)	−0.015(1)	−0.012(1)	−0.011(1)
	z	0.061(1)	0.063(1)	0.061(1)	0.059(1)
	SOF	0.93(1)	0.92(1)	0.88(1)	0.85(1)
Na(2)	x	0.816(2)	0.825(2)	0.826(2)	0.830(2)
	y	0.281(1)	0.281(1)	0.281(1)	0.282(1)
	z	0.192(1)	0.194(1)	0.194(1)	0.193(1)
	SOF	0.86(1)	0.76(1)	0.76(1)	0.68(1)
O(1)	x	0.638(3)	0.636(2)	0.639(2)	0.641(2)
	y	0.279(1)	0.272(1)	0.272(1)	0.273(1)
	z	0.042(1)	0.041(1)	0.040(1)	0.042(1)
O(2)	x	0.187(3)	0.195(2)	0.196(3)	0.194(2)
	y	0.454(2)	0.443(1)	0.438(1)	0.441(1)
	z	0.079(1)	0.086(1)	0.086(1)	0.084(1)
O(3)	x	0.218(2)	0.218(2)	0.222(2)	0.222(2)
	y	0.188(1)	0.191(1)	0.190(1)	0.192(1)
	z	0.171(1)	0.168(1)	0.167(1)	0.167(1)
O(4)	x	0.141(3)	0.127(2)	0.129(2)	0.124(2)
	y	0.480(1)	0.483(1)	0.485(1)	0.482(1)
	z	0.285(1)	0.285(1)	0.284(1)	0.282(1)
		Average values for SOF and B(Å^2)			
Fe/Si	SOF(Si)	0.10(2)	0.17(1)	0.17(1)	0.21(1)
	B	0.47(8)	0.50(6)	0.41(7)	0.13(7)
Na	SOF	0.90(1)	0.84(1)	0.82(1)	0.77(1)
	B	0.69(3)	1.60(13)	1.28(14)	1.53(14)
O	B	0.79(14)	1.01(11)	1.22(12)	0.80(12)
		Agreement indices			
R_{wp} (%)		9.52	8.88	9.15	8.69
R_B (%)		3.47	2.50	2.92	3.25
R_{exp} (%)		3.62	4.02	3.72	4.26

relationship to the corner-shared tetrahedral framework of cristobalite. O'Keeffe and Hyde (*13*) have demonstrated that rotation of the tetrahedra in the ideal high-cristobalite structure, *C*9, about particular combinations of $\bar{4}$ axes results in collapsing of the framework around the interstitial cavities to produce denser structures. One such rotation system gives rise to tetrahedral interstitial sites that share corners with the framework tetrahedra. Occupation of these sites gives the β-$NaFeO_2$ structure. The rotation angle ψ, given approximately as $\cos^{-1}[c^2/2ab]$ (*13*), is 33.3° for β-$NaFeO_2$. When ψ is increased to 45° the filled and interstitial sites have the same size and the wurtzite structure results.

The effect of SiO_2 substitution in β-$NaFeO_2$ on the cell parameters and atomic coordinates is shown in Table II. The unit cell volume decreases linearly with SiO_2 substitution but there is a marked anisotropy in the changes in individual cell parameters. The a and b parameters decrease whereas the c parameter increases with increasing SiO_2 content. The atomic displacements accompanying SiO_2 incorporation are shown (exaggerated for clarity) in Fig. 2b. The Fe and Na atoms undergo small displacements along [100] and [110], respectively. The oxygen atoms O(2) undergo the largest displacements and these occur in the *ac*-plane.

The movements of the oxygen atoms correspond to cooperative rotation of the tetrahedra about the *b*-axis. This type of rotation transforms the FeO_2 framework in β-$NaFeO_2$ to the high-cristobalite structure, for the same rotation angle ψ relative to *C*9. This can be seen by comparing O'Keeffe and Hyde's reported (*13*) systems of rotation axes applied to the (100) planes of tetrahedra at $x = -\frac{1}{4}$, 0, and $\frac{1}{4}$ in the *C*9 structure; the rotation axis for the tetrahedra at $x = \frac{1}{2}$ is included also in the following sequences:

(I) [00$\bar{1}$], [001], [00$\bar{1}$], [001] gives high-cristobalite;

(II) [0$\bar{1}$0], [001], [010], [00$\bar{1}$] gives low-cristobalite (γ-$NaFeO_2$);

(III) [00$\bar{1}$], [001], [010], [0$\bar{1}$0] gives β-$NaFeO_2$-type structures.

The difference between I and III is 0, 0, [0$\bar{1}\bar{1}$], [011], i.e., the two structures are interconverted by rotation of tetrahedra

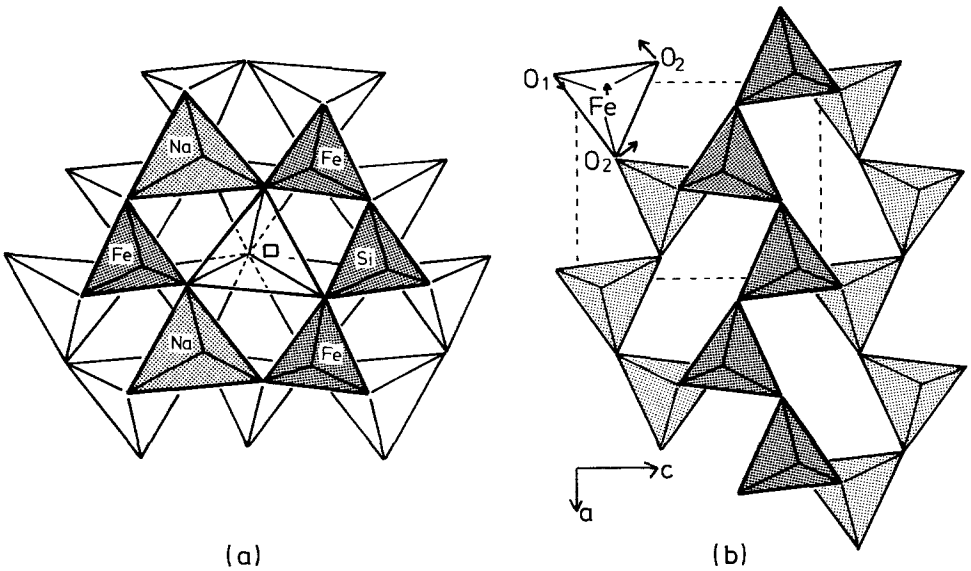

FIG. 2. Polyhedral representation of the β-$NaFeO_2$ structure viewed along [010]. In (a) both Na- and Fe-centered tetrahedra are shown to demonstrate the relationship to the wurtzite structure. The local substitution of Fe by Si together with the associated loss of Na is shown for $Na_{1-x}[Fe_{1-x}Si_x]O_2$. In (b) only Fe-centered tetrahedra are shown to emphasize the structural relationship to cristobalite.

about a face diagonal of the cubic *C*9 structure, equivalent to the *b*-axis of β-$NaFeO_2$. The rotation mechanism involves half of the tetrahedra, which form [100] chains in the alternate (010) planes of the β structure as shown in Fig. 2b. As discussed in Ref. (*13*) an additional small rotation is required to maintain connectivity in the β structure.

Note that the difference between II and III is $[0\bar{1}1]$, 0, 0, $[01\bar{1}]$ and so the interconversion of β- and γ-$NaFeO_2$ also involves rotation of half of the tetrahedra about axes parallel to $\langle 011 \rangle$ in *C*9. The rotations in this case are parallel to the *a*-axis of β-$NaFeO_2$, i.e., orthogonal to the axes involved in the β to high-cristobalite transformation (*1*).

For equal rotation angles the β and high-cristobalite structures have equal volumes (*13*). Using this, and the relationship between the cell parameters and the rotation angle (*13*), the calculated cell parameters for the high-cristobalite form of $NaFeO_2$ in the space group $I\bar{4}2d$ are a, $b = 5.06$, $c = 8.5$ Å. In order that a direct comparison can be made with the β structure, the tetragonal cell must be transformed as follows: $a' = \frac{1}{2}(a + b + c)$, $b' = \frac{1}{2}(a + b - c)$, $c' = (a - b)$, and $\gamma = 2 \tan^{-1} c/(a + b)$. The resulting cell parameters are a', $b' = 5.55$, $c' = 7.15$ Å, $\gamma = 100°$. This monoclinic cell for high-cristobalite has the same orientation as the β phase cell and is illustrated in Fig. 3a. It is seen that the transformation from the β phase to high-cristobalite by rotation about *b* also involves a translation of alternate (010) planes along [100]. For the limiting case of a rotation angle of 45°, for which the β phase has the wurtzite structure, the translation is almost 2 Å and the hexagonal close packing of anions is converted to cubic close packing as described in Ref. (*13*).

In the $NaFeO_2$–SiO_2 solid solutions the rotation of tetrahedra about *b* is constrained to obey the space group symmetry of the β phase. This requires that the [100] chains of tetrahedra in successive (010)

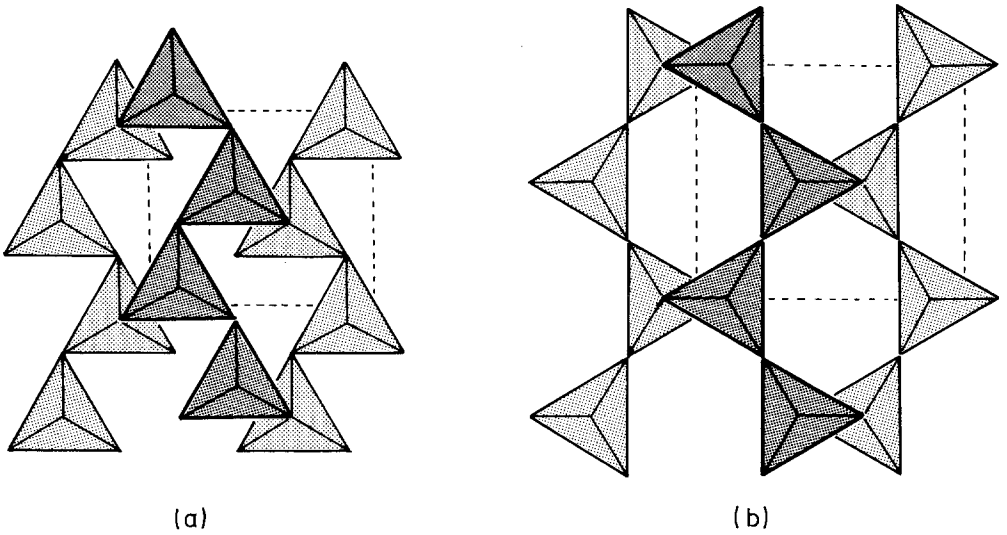

FIG. 3. (a) The high-cristobalite structure viewed in terms of a monoclinic cell, transformed from the parent cell (see text), for direct comparison to the β-$NaFeO_2$ structure. (b) Rotation of FeO_4 tetrahedra of β-$NaFeO_2$ about [010] by 30° constrained to the space group symmetry.

planes are rotated in conformity with the 2_1 screw axis, and that the translations along [100] are of equal and opposite magnitude for successive (010) planes. For the limiting case when the β phase has $\psi = 45°$ (wurtzite) the change in β cell parameters as a function of the rotation angle can be easily derived:

$$a = (\sqrt{3} \cos \alpha + \sin \alpha)0\text{–}0$$

$$c = 1/\sqrt{3} \cos(30 - \alpha)0\text{–}0,$$

where α is the rotation about b and 0–0 is the tetrahedral edge (regular tetrahedra). The rotation involves an expansion of both a and c for the β cell, which attain maximum values for wurtzite at a rotation angle of 30°. The resulting intermediate structure is shown in Fig. 3b. Increasing the rotation angle to 60° produces either a twin orientation of the β phase or the high-cristobalite structure with $\psi = 45°$, depending on the relative senses of rotation of the [100] chains of tetrahedra.

The above equations give an approximate estimate of the change in cell parameters in the $NaFeO_2$–SiO_2 β solid solutions. For the maximum silica incorporation of 10 mol%, the coordinate changes for O(2) in Table II correspond to a rotation about b of about 3°. The calculated increases in a and c are 0.17 and 0.20 Å, respectively, using an 0–0 value of 3.42 Å (average for the FeO_4 and NaO_4 tetrahedra in β-$NaFeO_2$). The actual cell parameter increases due to tetrahedra rotation will be slightly smaller than these values based on the wurtzite limit of the β phase. The experimental cell parameters for the β series in Table II show that the c-axis expansion is only 0.04 Å and the a-axis actually contracts by 0.10 Å when 10 mol% of iron is replaced by silicon. The effect of change of cation size thus overrides the effect due to tetrahedral rotation.

3.1.2. Interatomic distance and angle changes in the β series. Selected interatomic distances and angles for the β solid solution phases are given in Table V. The incorporation of SiO_2 involves a progressive decrease in M–O, M = Fe,Si, and increase in Na–O. The increase in the aver-

TABLE V

SELECTED INTERATOMIC DISTANCES AND ANGLES FOR β_{ss}-SOLID SOLUTIONS OF COMPOSITION $Na_{1-x}[Fe_{1-x}Si_xO_2]$[a]

	x in $Na_{1-x}[Fe_{1-x}Si_xO_2]$				
	0.00	0.025	0.050	0.075	0.100
			Distances (Å)		
M–O(1)	1.859(7)	1.860(7)	1.861(8)	1.833(10)	1.855(15)
M–O(1)	1.895(12)	1.870(10)	1.871(10)	1.857(7)	1.876(10)
M–O(2)	1.885(13)	1.867(8)	1.848(9)	1.845(7)	1.807(11)
M–O(2)	1.889(9)	1.885(11)	1.880(12)	1.864(9)	1.820(13)
Mean	⟨1.882⟩	⟨1.871⟩	⟨1.865⟩	⟨1.850⟩	⟨1.840⟩
Na–O(1)	2.28(2)	2.29(1)	2.29(1)	2.30(1)	2.26(2)
Na–O(1)	2.31(1)	2.30(1)	2.30(2)	2.33(1)	2.32(2)
Na–O(2)	2.29(2)	2.30(1)	2.31(2)	2.34(1)	2.40(2)
Na–O(2)	2.37(1)	2.40(1)	2.40(2)	2.41(1)	2.46(2)
Mean	⟨2.31⟩	⟨2.32⟩	⟨2.33⟩	⟨2.35⟩	⟨2.36⟩
O. . .O(min)	3.02(1)	3.01(1)	2.99(1)	2.99(1)	2.98(2)
M. . .*M*(min)	3.329(5)	3.328(4)	3.325(5)	3.314(4)	3.288(7)
M. . .Na(min)	3.26(1)	3.24(1)	3.24(1)	3.22(1)	3.19(2)
Na. . .Na(min)	3.32(1)	3.31(1)	3.30(1)	3.31(1)	3.30(2)
			Angles (°)		
O(1)–*M*–O(1)	107.8(3)	107.9(3)	107.9(3)	107.6(3)	107.1(7)
O(1)–*M*–O(2)	107.8(5)	107.8(4)	107.5(5)	107.6(3)	107.6(6)
O(1)–*M*–O(2)	108.1(4)	107.9(4)	107.8(5)	108.3(4)	108.1(6)
O(1)–*M*–O(2)	113.3(5)	112.1(4)	112.0(5)	112.5(4)	112.5(6)
O(1)–*M*–O(2)	108.0(5)	109.4(4)	109.8(5)	108.5(4)	109.9(6)
O(2)–*M*–O(2)	112.1(4)	111.5(3)	111.7(4)	111.1(3)	111.5(6)
Mean	⟨109.4⟩	⟨109.4⟩	⟨109.5⟩	⟨109.3⟩	⟨109.5⟩
O(1)–Na–O(2)	126.6(5)	127.9(4)	128.0(5)	129.8(4)	131.1(6)
O(1)–Na–O(1)	104.4(5)	105.3(5)	105.0(6)	105.1(4)	104.6(7)
O(1)–Na–O(2)	105.5(6)	104.4(5)	104.0(6)	103.8(5)	102.0(7)
O(2)–Na–O(1)	107.4(6)	106.7(5)	107.2(6)	105.9(4)	107.2(7)
O(2)–Na–O(2)	106.1(6)	106.3(5)	106.9(6)	106.6(5)	107.6(7)
O(1)–Na–O(2)	105.1(4)	103.9(5)	103.3(4)	102.7(3)	100.3(5)
Mean	⟨109.2⟩	⟨109.1⟩	⟨109.1⟩	⟨109.0⟩	⟨108.8⟩
M–O(1)–*M*	125.8(6)	126.5(6)	125.9(6)	128.1(6)	126.0(7)
M–O(2)–*M*	123.7(7)	125.2(6)	126.2(7)	126.5(4)	130.2(7)
Na–O(1)–Na	94.4(5)	93.9(5)	94.2(6)	92.1(5)	93.0(6)
Na–O(2)–Na	91.1(6)	89.6(5)	88.7(5)	88.3(3)	85.6(6)

[a] The Fe and mixed Fe/Si site denoted by *M*.

age Na–O bond length results from the *b*-axis rotation of the tetrahedral framework leading to an expansion of the interstitial cavity volume. This expansion is more than offset by the contraction of the framework tetrahedra and so the overall effect of SiO_2 incorporation is a cell volume decrease. This is plotted in Fig. 4, together

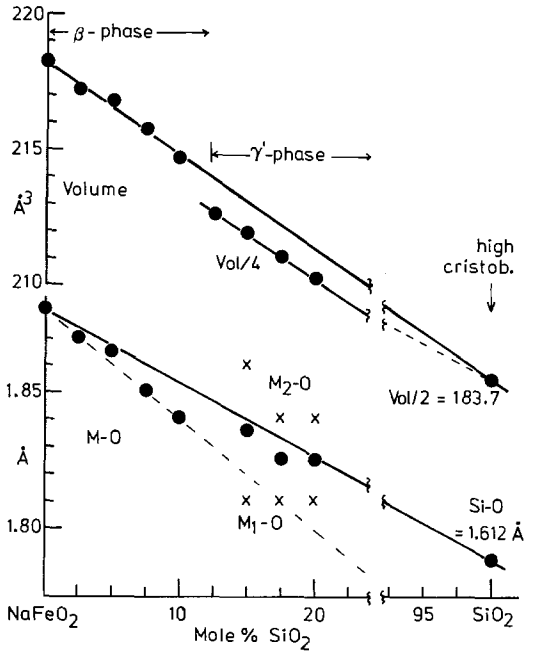

FIG. 4. A plot of unit cell volume of $Na_{1-x}[Fe_{1-x}Si_x]O_2$ solid solutions against x. A plot of average M–O bond lengths as a variation of Si substitution is also included together with the data points for the two independent M sites of the γ'_{ss} phases and that for high-cristobalite.

with the variation in the average M–O bond length as a function of Si substitution. Also included in Fig. 4 are data points for the γ'_{ss} solid solution phases and for the end member SiO_2 (high-cristobalite form). Whereas the plotted volumes for the β phases extrapolate smoothly to that for SiO_2, the average M–O distances show a deviation from the line drawn between $NaFeO_2$ and SiO_2 which increases with increasing SiO_2 content. In contrast the points for the γ'_{ss} phases fit closely to the line. Thus in the β phases the contraction in the framework tetrahedra bond lengths is significantly greater than expected from substitution of Si for Fe.

The interpretation of the observed macroscopic crystallographic changes in the β phase series requires a consideration of the local atomic displacements when Si replaces Fe + Na in $Na_{1-x}[Fe_{1-x}Si_x]O_2$. We will assume that the Si substitution and Na loss are strongly coupled and occur at adjacent framework and interstitial sites, see Fig. 2a, giving O_3–□–O–Si–O_3 (□ = Na vacancy). The seven anions affected by the substitution are linked to a further 20 NaO_4 and FeO_4 tetrahedra and so the structural response to the local charge imbalance is spread over a relatively large volume. The substitution of Si for Fe + Na gives rise to the following seven anion coordinations:

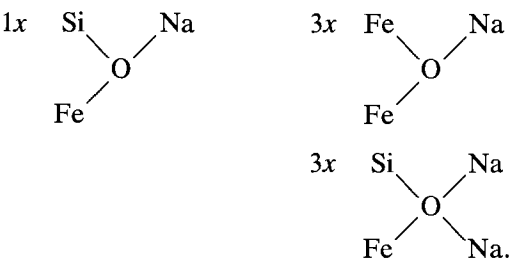

In the first of these the Pauling electrostatic valence rule is satisfied and so the bond lengths should be close to normal. The reduction in cation packing around the anion from four to three allows the Fe–O–Si angle to increase, thus reducing the nonbonded repulsion between the Fe and Si atoms. The next group of three anions also have three cation neighbors and there will be an increase in the Fe–O–Fe angle. These anions are undersaturated because the loss of Na is not compensated by Si substitution. Bond shortening will occur to redress the local charge imbalance. This is expected to occur predominantly in the two Fe–O bonds because any Na–O bond shortening will work in opposition to the expansion of the interstitial site volume resulting from an increase in M–O–M. The third group of anions involves four cation neighbors as in $NaFeO_2$ and so there will be little change in the M–O–M angle. However, the substitution of Si for Fe results in an excess of positive charge at the anion sites which will be locally compensated by

increased bond lengths to the cations. In this case lengthening of Na–O is compatible with an interstitial volume increase and so the major bond length increases are expected to occur for Na–O.

These local structural adjustments to the substitution of Si for Fe + Na are consistent with the observed macroscopic bond length and angle changes. The results given in Table V show that the major changes are associated with O(2), which connects pairs of MO_4 tetrahedra in the *ac*-plane, see Fig. 2b. This suggests that O(2) links SiO_4 tetrahedra with vacant tetrahedral interstitial sites as shown in Fig. 2a. It is interesting to note that if O(1) was involved in the same type of linkage then the local increase in the Fe–O(1)–Si angle would require rotation of the tetrahedra about the *a*-axis. As discussed in the previous section this leads to the γ form of Na(Fe, Si)O_2 (low-cristobalite). For equal rotation angles (relative to the *C*9 structure) the low-cristobalite structure is less dense than high-cristobalite and so is not favored by Si substitution.

The local strains introduced into the $NaFeO_2$ matrix by the coupled substitution Si = Fe + Na increase with extent of replacement until eventually the β solid solution becomes unstable relative to the γ'_{ss} structure-type, which has more flexibility to adjust to the changes. This is accomplished by ordering of Si, Fe and Na, □ in separate crystallographic sites as discussed below.

3.2. γ'_{ss}-Solid Solutions

3.2.1. Relationship to the C9 structure. The structure of the γ'_{ss} phases is isotypic with that of $KFeO_2$ and $KGaO_2$ (*3, 12*). As for the β_{ss}- and γ_{ss}-solid solutions the connectivity of the MO_4 tetrahedral units of the MO_2 framework of the γ'_{ss} solid solutions involves only corner linking and its overall structure may be described as a collapsed high-cristobalite structure. The extent of the deformation from the parent *C*9 structure is far greater for the γ'_{ss} solid solutions than for $KFeO_2$ and $KGaO_2$, resulting in tetrahedral coordination for the sodium cations, analogous to that in the β_{ss} and γ_{ss} phases.

The MO_2 framework in the γ'_{ss} phases can be derived from that of ideal high-cristobalite by considering rotations of all tetrahedra about two sets of $\bar{4}$ axes of the *C*9 structure. This approach was developed by O'Keeffe and Hyde (*13*) for those *C*9-derived structures that could be generated by rotation operations performed on the contents of one *C*9 unit cell, *viz.* high- and low-cristobalite and β-$NaFeO_2$. The relationship of the structure of γ'_{ss} to *C*9 is more complex and the contents of eight unit cells of the *C*9 structure have to be considered to obtain a full description.

The patterns of rotation axes within the *Fd3m* cell of the *C*9 structure required to generate the γ'_{ss} structure are shown in Fig. 5, using the same notations as employed by O'Keeffe and Hyde in their Fig. 2 (*13*). The major difference between the rotation system in the γ'_{ss} phases and those in the structures considered by O'Keeffe and Hyde is that in the latter cases each of the tetrahedra whose centers fall on a line parallel to $[\bar{1}10]_c$ possesses a common rotation axis and operation. In γ'_{ss}, half of the $[\bar{1}10]_c$ strings of tetrahedra have rotation axes that are alternatively parallel to $[010]_c$ and $[001]_c$. Although eight unit cells of the *C*9 structure are required to describe the tetrahedra rotations in the γ'_{ss} structure, the unit cell of the latter is only twice the volume of that for *C*9. The γ'_{ss} unit cells *a* and *b* are parallel to $\langle 110\rangle_c$ and are outlined in Fig. 5.

3.2.2. Descriptions of the MO_2 framework in γ'_{ss}. A projection of a polyhedral representation of the MO_2 framework down $[100]_{\gamma'}$ is shown in Fig. 6a. This direction corresponds to a $\langle 110\rangle$ direction in the *C*9 structure. A striking feature of the structure is the two distinct types of framework cavities which closely resemble those found in

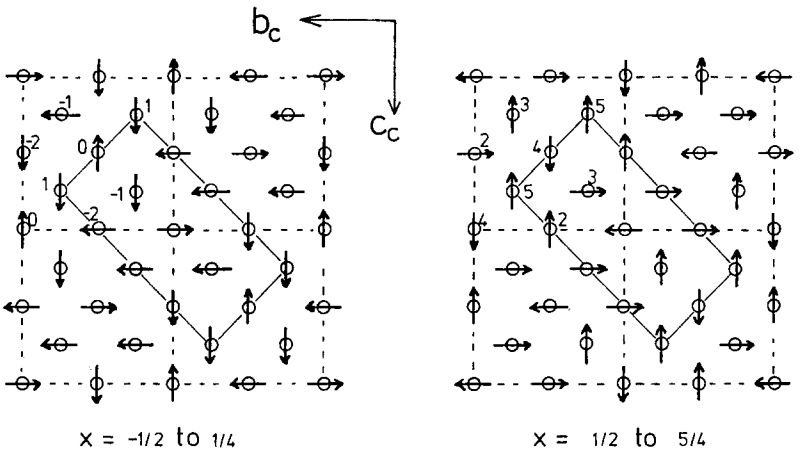

FIG. 5. Patterns of rotation axes within the *Fd3m* cell of the *C*9 structure required to produce the γ'_{ss} structure. Only centers of the tetrahedra are shown; notation as in legend to Fig. 2 of Ref. (*13*). Heights in multiples of *a*/4 are shown.

β-$NaFeO_2$ (triangular cross section) and in γ-$NaFeO_2$ (rhombic cross section). The equivalent views of the latter two structures are shown for comparison in Fig. 6b. At first sight this suggests that the structure is an ordered intergrowth of the β_{ss} and γ_{ss} structures, each of which can be readily derived from *C*9 by a rotation sequence defined by O'Keeffe and Hyde. However, closer examination reveals that the orientation of half of the MO_4 tetrahedra along $[100]_{\gamma'}$ for the hypothetical intergrowth model, Fig. 6c, is opposite to that for the real γ'_{ss} structure. These require a further rotation about a direction parallel to $\langle 110\rangle_c$ ($=[010]_{\gamma'}$) to generate the γ'_{ss} framework as indicated in Fig. 6c. As described in Section 3.1.1 application of this type of rotation transforms the MO_2 framework in β-$NaFeO_2$ to that in high-cristobalite, and γ-$NaFeO_2$, to that in β-$NaFeO_2$. The MO_2 framework in the γ'_{ss} phases can thus be regarded as a complex intergrowth of elements of β, γ, and high-cristobalite.

Some evidence was obtained that suggests that the hypothetical β–γ intergrowth structure shown in Fig. 6c may occur as an intermediate in the formation of the γ'_{ss} phases, or in their transformation to cubic δ phases (*1*). For example when the composition $Na_{0.61}Fe_{0.61}Si_{0.39}O_2$ was heated at a temperature just below that of the γ' to δ phase transition the XRD pattern of the quenched product showed selective broadening of the γ'_{ss} phase reflections with k odd, Fig. 7a. These reflections are superlattice reflections relative to the *C*9 unit cell and may be ascribed to tetrahedral rotations about $[010]_{\gamma'}$. These rotations result in a doubling of the 5.5 Å axis of the hypothetical intergrowth structure in Fig. 6c to produce the structure shown in Fig. 6a. In contrast the superlattice reflections with l odd, ascribed to the β–γ-type intergrowth along $[001]_{\gamma'}$, remain sharp. For comparison the XRD pattern of $Na_{0.61}Fe_{0.61}Si_{0.39}O_2$, heated to a temperature away from γ' to δ transition, shown in Fig. 7b, reveals a fully ordered γ'_{ss} structure.

3.2.3. Sodium coordination in γ'_{ss}. In common with the β_{ss} and γ_{ss} phases, the γ'_{ss} phases have tetrahedral coordination of the sodium atoms. Relative to the *C*9 structure there has been severe collapse of the MO_2

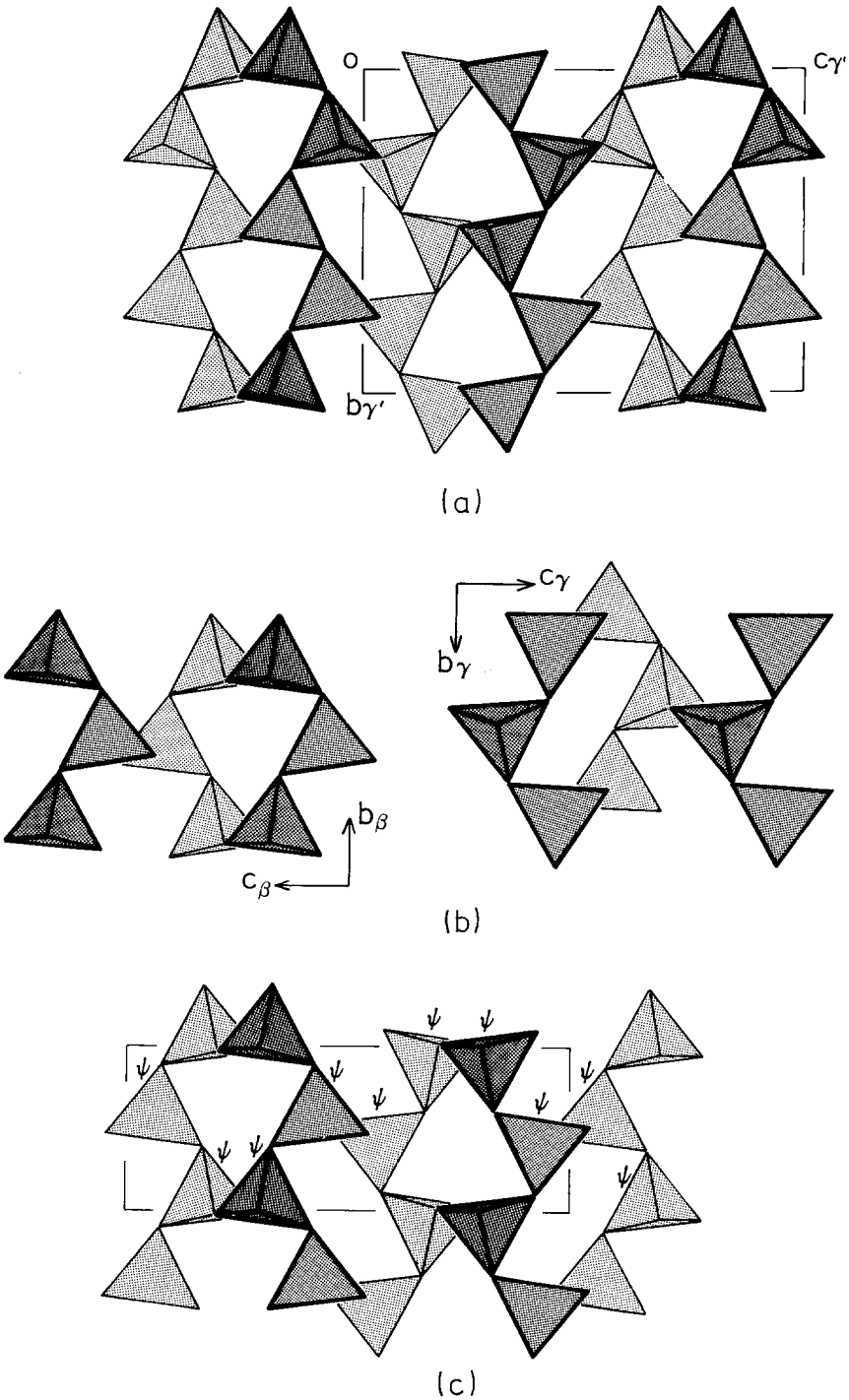

FIG. 6. (a) The MO_2 tetrahedral framework in the γ'_{ss} phase viewed along $[100]_{\gamma'}$. (b) Equivalent representations for the β and γ structures. (c) Hypothetical intergrowth of β and γ structures, having the same [100] projection as the γ'_{ss} phase. Tetrahedral rotations about [010] to convert this structure to that of γ'_{ss} are shown.

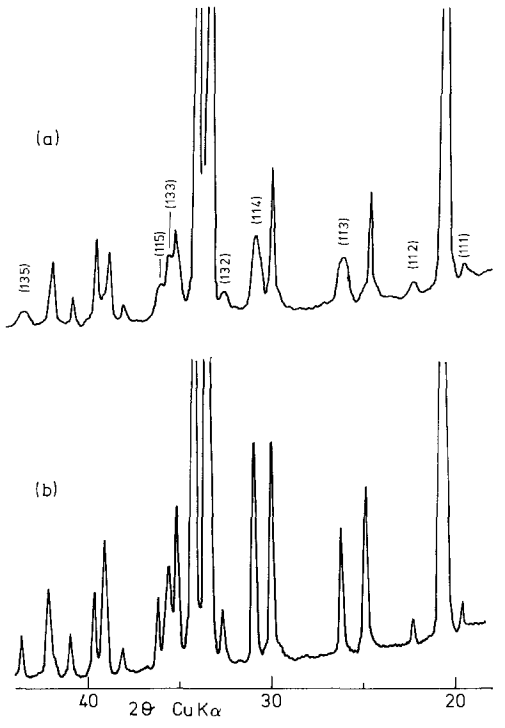

FIG. 7. Powder XRD patterns for a γ'_{ss} phase with $x = 0.39$: (a) Heated to a temperature just below γ' to δ transition, showing selective broadening of reflections with k odd. (b) Heated to a temperature substantially below the transition temperature, showing fully ordered γ'_{ss}.

framework around the cavity sites, resulting in four Na–O distances less than about 2.5 Å and with the next nearest oxygens greater than 3 Å away.

The articulation of the NaO_4 tetrahedra in γ'_{ss} is quite different from that in the β_{ss} and γ_{ss} phases. In the structures of the latter two phases the NaO_4 tetrahedra share corners only to form chains along $[010]_{\beta,\gamma}$, analogous to the chains of MO_4 framework tetrahedra shown in Fig. 6b. In the γ'_{ss} phases tetrahedral edge sharing occurs, both between $Na(1)O_4$ and $Na(2)O_4$ tetrahedra and between pairs of $Na(1)O_4$ tetrahedra, giving clusters of four edge-shared tetrahedra as shown in Fig. 8. These clusters are linked together *via* corner sharing between $Na(2)O_4$ tetrahedra along $[100]_{\gamma'}$ producing undulating $(010)\gamma'$ sheets (see Fig. 8). The change in NaO_4 tetrahedra articulation from the β_{ss} and γ_{ss} phases to the γ'_{ss} phases involves a displacement along [010] of half of the sodium atoms through the tetrahedra bases into the adjacent empty tetrahedral sites.

Although having the same primary coordination of the cations by oxygen, the β_{ss}, γ_{ss}, and γ'_{ss} phases display interesting variations in the cation distributions around cation sites. In the β_{ss} phases both Na and Fe/Si have 12 nearest neighbor cations at distances in the range 3.2 to 3.6 Å, with the next-nearest neighbors being more than 4.4 Å away. In the γ_{ss} phases there are 11 nearest neighbor cations at distances in the range 3.2 to 3.7 Å plus two further neighbors at 4.0 Å, and then a jump to 4.7 Å for the next nearest cations. The cations in the γ'_{ss} phases have 13 nearest neighbor cations at distances typically in the range 3.0 to 3.8 Å and with the next nearest cations at distances of more than 4.3 Å. The increasing nearest neighbor cation coordination from γ_{ss} to β_{ss} to γ'_{ss} are in accord with the stability fields for these phases. Relative to the β_{ss} phases the γ_{ss} phases are stable at higher temperatures (equivalent to lower pressures) while the γ'_{ss} phases are stabilized by increasing substitution of Fe by Si (equivalent to higher pressures).

3.2.4. Fe/Si and Na/□ ordering in γ'_{ss}. The substitution of SiO_2 into $NaFeO_2$ involves both replacement of Fe by Si in the framework tetrahedra and removal of Na from the framework cavities. The structure of the γ'_{ss} phases contains two independent sites for both the framework and the cavity cations and the results of the structure refinements, given in Table IV, show there is a partial ordering of Fe/Si and Na/□ in these sites. Silicon preferentially orders into the $M(1)$ sites while vacancies are ordered predominantly at the Na(2) sites. The results of the structure refinements are sup-

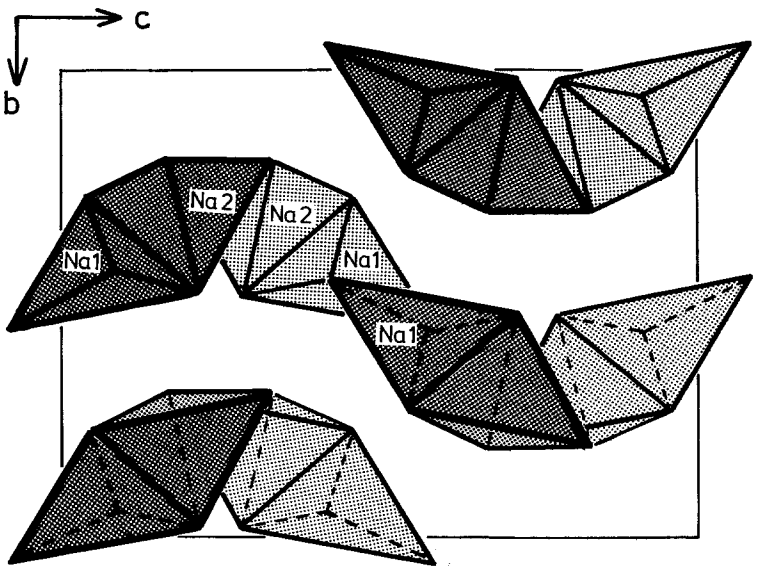

FIG. 8. The articulation of the NaO_4 tetrahedra in the γ'_{ss} structure viewed along $[100]_{\gamma'}$ showing the corner and edge sharing arrangement characteristic of this structure. Light and dark stippling correspond to tetrahedra centered at approximately $x = \frac{1}{4}$ and $\frac{3}{4}$, respectively.

ported by the bond length differences as shown by the results in Table VI. For the highest SiO_2-containing phase studied, $Na_{0.8}Fe_{0.8}Si_{0.2}O_2$, site Na(2) is only 68% occupied by sodium whereas site Na(1) has 85% occupation. The Na/□ results are correlated with the Fe/Si ordering. While both Na(1) and Na(2) have nine nearest neighbor M cations, Na(1) has $4M(1) + 5M(2)$ whereas Na(2) has $5M(1) + 4M(2)$. The silicon-rich $M(1)$ sites are thus more closely associated with the Na(2) sites which have the higher vacancy concentrations.

The location of the Na(1)- and Na(2)-centered tetrahedra within the MO_2 framework is viewed along $[100]_{\gamma'}$ in Fig. 9. When compared with Fig. 6a it is seen that the Na(1) atoms occupy the framework cavities with rhombic cross sections and the Na(2) atoms occupy cavities with triangular cross sections. The latter cavities resemble most closely those in high-cristobalite and it is in this part of the γ'_{ss} structures that the major Fe/Si substitution and cavity vacancy concentrations occur. The bond lengths and angles associated with the different NaO_4 tetrahedra are compared in Table VI.

It is interesting to enquire why the γ'_{ss} structure is able to accommodate changes in the Fe/Si ratio with essentially isotropic changes to the unit cell dimensions whereas similar compositional changes in the β_{ss} phases result in extremely anisotropic changes to the cell parameters as seen by comparing the results in Tables II and IV. The β_{ss} phases have only one type of framework cavity and as described in Section 3.1.1, changes to its dimensions occur by cooperative rotation of the framework tetrahedra. In contrast the structures of the γ'_{ss} phases contain intergrowths of two types of cavities. The $[100]_{\gamma'}$ projected cross sections are identical with those in the γ_{ss} phases (rhombic) and β_{ss} (triangular) and as previously discussed (*1*) these two structure types can be interconverted by rotation about $[100]_{\gamma'}$. The $[010]_{\gamma'}$ projection also comprises intergrowths of

TABLE VI

SELECTED INTERATOMIC DISTANCES AND ANGLES FOR γ'_{ss}-SOLID SOLUTIONS OF COMPOSITION $Na_{1-x}[Fe_{1-x}Si_xO_2]$[a]

	x in $Na_{1-x}[Fe_{1-x}Si_xO_2]$								
	0.125	0.150	0.175	0.200		0.125	0.150	0.175	0.200
	Distances (Å)				*M*. . .Na(min)	3.16(1)	3.16(1)	3.13(1)	3.09(1)
M(1)–O(2)	1.90(2)	1.84(1)	1.86(1)	1.89(1)	Na. . .Na(min)	2.88(2)	2.92(2)	2.89(2)	2.88(2)
M(1)–O(3)	1.77(1)	1.80(1)	1.78(1)	1.79(1)					
M(1)–O(4)	1.75(2)	1.78(1)	1.75(1)	1.75(1)		Angles (°)			
M(1)–O(4)	1.90(2)	1.83(1)	1.86(1)	1.83(1)	O(2)–*M*(1)–O(3)	104.4(8)	109.0(6)	110.3(6)	108.5(6)
Mean	⟨1.83⟩	⟨1.81⟩	⟨1.81⟩	⟨1.81⟩	O(2)–*M*(1)–O(4)	112.9(7)	109.9(6)	109.7(7)	108.2(6)
					O(2)–*M*(1)–O(4)	113.2(7)	110.9(6)	110.4(7)	110.7(6)
M(2)–O(1)	1.80(2)	1.78(1)	1.79(1)	1.81(1)	O(3)–*M*(1)–O(4)	110.6(6)	110.4(5)	110.2(6)	111.5(6)
M(2)–O(1)	1.85(2)	1.81(1)	1.82(1)	1.81(1)	O(3)–*M*(1)–O(4)	111.3(5)	110.8(5)	110.8(5)	112.6(5)
M(2)–O(2)	2.04(2)	1.93(1)	1.87(1)	1.90(1)	O(4)–*M*(1)–O(4)	104.6(5)	105.7(4)	105.4(4)	105.3(4)
M(2)–O(3)	1.94(2)	1.90(1)	1.88(1)	1.87(1)	Mean	⟨109.5⟩	⟨109.5⟩	⟨109.5⟩	⟨109.5⟩
Mean	⟨1.91⟩	⟨1.86⟩	⟨1.84⟩	⟨1.84⟩					
					O(1)–*M*(2)–O(1)	112.1(5)	112.2(4)	110.9(4)	111.7(4)
Na(1)–O(1)	2.29(2)	2.45(2)	2.48(2)	2.46(2)	O(1)–*M*(2)–O(2)	108.5(6)	111.7(5)	111.6(6)	111.3(6)
Na(1)–O(2)	2.18(2)	2.27(2)	2.28(2)	2.22(2)	O(1)–*M*(2)–O(2)	104.5(6)	105.6(5)	106.2(6)	105.4(6)
Na(1)–O(2)	2.25(2)	2.32(2)	2.29(2)	2.28(2)	O(1)–*M*(2)–O(3)	113.4(6)	113.8(5)	114.6(6)	114.9(5)
Na(1)–O(4)	2.37(2)	2.38(2)	2.42(2)	2.48(2)	O(1)–*M*(2)–O(3)	112.3(6)	111.4(6)	110.9(4)	110.7(6)
Mean	⟨2.27⟩	⟨2.35⟩	⟨2.38⟩	⟨2.36⟩	O(2)–*M*(2)–O(3)	105.3(6)	101.4(5)	102.4(6)	102.3(6)
					Mean	⟨109.4⟩	⟨109.4⟩	⟨109.4⟩	⟨109.4⟩
Na(2)–O(1)	2.39(2)	2.46(2)	2.47(2)	2.43(2)					
Na(2)–O(3)	2.30(3)	2.31(2)	2.32(2)	2.33(2)	O(2)–Na(1)–O(2)	93.7(8)	99.1(6)	101.7(7)	100.5(6)
Na(2)–O(3)	2.41(2)	2.36(2)	2.38(2)	2.35(2)	O(2)–Na(1)–O(4)	100.6(8)	102.5(6)	101.0(7)	100.2(7)
Na(2)–O(4)	2.37(2)	2.44(2)	2.46(2)	2.44(2)	O(2)–Na(1)–O(1)	102.8(7)	99.0(5)	96.6(6)	96.3(6)
Mean	⟨2.37⟩	⟨2.40⟩	⟨2.40⟩	⟨2.39⟩	O(2)–Na(1)–O(4)	157.0(8)	153.7(6)	152.9(7)	155.2(7)
					O(2)–Na(1)–O(1)	103.4(9)	101.6(6)	102.6(7)	103.6(7)
O(1)–Fe(2)	1.80(2)	1.78(1)	1.79(1)	1.81(1)	O(4)–Na(1)–O(1)	90.9(7)	89.8(5)	89.3(6)	87.4(6)
O(1)–Fe(2)	1.85(2)	1.81(1)	1.82(1)	1.81(1)	Mean	⟨108.0⟩	⟨107.6⟩	⟨107.4⟩	⟨107.2⟩
O(1)–Na(1)	2.30(2)	2.45(2)	2.48(2)	2.46(2)					
O(1)–Na(2)	2.40(2)	2.46(2)	2.47(2)	2.43(2)	O(3)–Na(2)–O(3)	98.0(7)	101.0(6)	100.7(7)	101.3(7)
					O(3)–Na(2)–O(4)	100.0(7)	99.3(6)	99.0(7)	96.8(7)
O(2)–Fe(1)	1.90(2)	1.84(1)	1.86(1)	1.89(1)	O(3)–Na(2)–O(1)	134.8(7)	132.4(6)	133.1(6)	132.5(6)
O(2)–Fe(2)	2.04(2)	1.93(1)	1.87(1)	1.90(1)	O(3)–Na(2)–O(4)	138.7(7)	141.2(6)	140.8(7)	142.3(7)
O(2)–Na(1)	2.18(2)	2.27(2)	2.28(2)	2.22(2)	O(3)–Na(2)–O(1)	103.9(7)	102.0(6)	101.5(7)	102.1(7)
O(2)–Na(1)	2.25(2)	2.32(2)	2.29(2)	2.28(2)	O(4)–Na(2)–O(1)	88.8(7)	87.9(5)	88.9(6)	89.0(6)
					Mean	⟨110.7⟩	⟨110.6⟩	⟨110.7⟩	⟨110.7⟩
O(3)–Fe(1)	1.77(1)	1.80(1)	1.78(1)	1.79(1)					
O(3)–Fe(2)	1.94(1)	1.90(1)	1.88(1)	1.87(1)	Fe(2)–O(1)–Fe(2)	127(1)	129(1)	129(1)	128(1)
O(3)–Na(2)	2.30(2)	2.31(2)	2.32(2)	2.34(2)	Na(1)–O(1)–Na(2)	76(1)	73(1)	74(1)	75(1)
O(3)–Na(2)	2.41(2)	2.36(2)	2.38(2)	2.35(2)					
					Fe(1)–O(2)–Fe(2)	113(1)	120(1)	123(1)	121(1)
O(4)–Fe(1)	1.75(2)	1.78(1)	1.75(1)	1.75(1)	Na(1)–O(2)–Na(1)	87(1)	81(1)	78(1)	80(1)
O(4)–Fe(1)	1.90(2)	1.83(1)	1.85(1)	1.83(1)	Fe(1)–O(3)–Fe(2)	129(1)	129(1)	130(1)	130(1)
O(4)–Na(2)	2.37(2)	2.44(2)	2.46(2)	2.44(2)	Na(2)–O(3)–Na(2)	85(1)	85(1)	84(1)	85(1)
O(4)–Na(1)	2.37(2)	2.38(2)	2.42(2)	2.48(2)					
					Fe(1)–O(4)–Fe(1)	126(1)	128(1)	129(1)	129(1)
O. . .O(min)	2.88(1)	2.88(1)	2.87(1)	2.84(1)	Na(2)–O(4)–Na(1)	75(1)	75(1)	75(1)	74(1)
M. . .*M*(min)	3.241(7)	3.249(5)	3.248(6)	3.229(5)					

[a] Mixed Fe/Si sites denoted by *M*(1) and *M*(2).

rhombic and triangular cross sections which can be interconverted by rotation about $[010]_{\gamma'}$. Thus in the γ'_{ss} phases the tetrahedral rotations accompanying Fe/Si and Na/□ substitutions result in compensating changes to the dimensions of the two types of cavities and so to a first approximation the overall unit cell shape is not significantly changed. The main changes in cell dimensions are then essentially isotropic due to changes in the size of the framework cations.

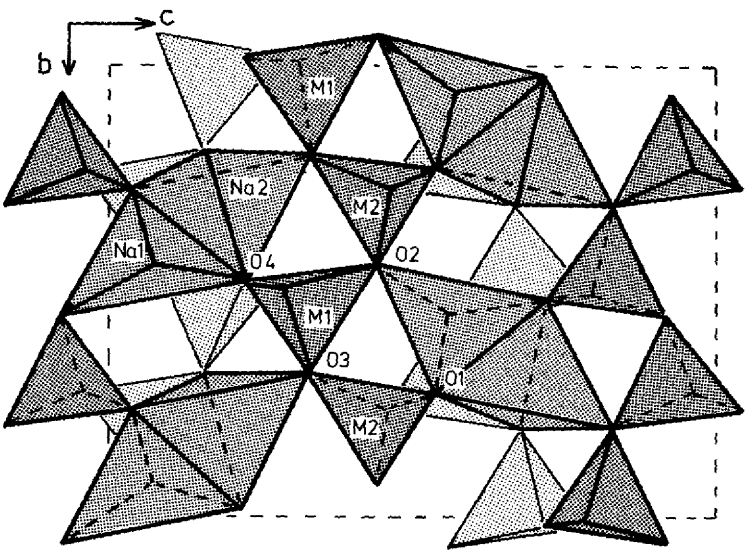

FIG. 9. The $Na(1)O_4$ and $Na(2)O_4$ tetrahedra within the MO_2 framework of the γ'_{ss} structure viewed along $[100]_{\gamma'}$. Light and dark stippling correspond to tetrahedra centered at approximately $x = \frac{1}{4}$ and $\frac{3}{4}$, respectively.

Acknowledgment

We thank the University of Melbourne for the award of a Special Studies Programme to B.F.H.

References

1. I. E. GREY AND C. LI, *J. Solid State Chem.* **69,** 116 (1987).
2. G. H. COVEY, *Pulp Pap. Canada* **83,** 92 (1982).
3. E. VIELHABER AND R. HOPPE, *Z. Anorg. Allg. Chem.* **369,** 14 (1969).
4. D. B. WILES AND R. A. YOUNG, *J. Appl. Crystallogr.* **14,** 149 (1981).
5. R. J. HILL AND C. J. HOWARD, *J. Appl. Crystallogr.* **18,** 173 (1985).
6. G. CAGLIOTTI, A. PAOLETTI, AND F. P. RICCI, *Nucl. Instrum.* **3,** 223 (1958).
7. H. M. RIETVELD, *J. Appl. Crystallogr.* **2,** 65 (1969).
8. R. J. HILL AND I. C. MADSEN, *J. Electrochem. Soc.* **131,** 1486 (1984).
9. "International Tables for X-ray Crystallography," Vol. IV, Kynoch Press, Birmingham, UK (1974).
10. E. F. BERTAUT, A. DELAPALME, AND G. BASSI, *J. Phys.* **25,** 545 (1964).
11. G. M. SHELDRICK, "SHELX-76, Program for Crystal Structure Determination," University of Cambridge, UK (1976).
12. Z. TOMKOWICZ AND A. SZYULA, *J. Phys. Chem. Solids* **38,** 1117 (1977).
13. M. O'KEEFFE AND B. G. HYDE, *Acta Crystallogr., Sect. B* **32,** 2923 (1976).